RSC Advances

PAPER

View Article Online
View Journal | View Issue

Cite this: *RSC Adv.*, 2026, **16**, 11259

Enhanced visible-light-driven photocatalytic degradation of methylene blue and ciprofloxacin using magnetic $NiFe_2O_4$@ZIF 67

Anulipsa Priyadarshini,†[a] Niharika Das,†[a] Saraswati Soren,†[a] Swasti Padma Panda,[a] Subrat Swain,[a] Jagannath Panda,[ab] Bikash Chandra Dhal,[a] Jaykishon Swain,[a] Debashis Acharya,[a] Srabanti Ghosh[c] and Rojalin Sahu *[a]

Designing metal organic framework (MOF)-based stable heterostructures remains a challenging task for material scientists. Herein, a magnetic photocatalyst, designated 30NFZ67, was synthesized using a simple and green method by combining ZIF 67 and $NiFe_2O_4$ at room temperature. The fabrication of a hybrid MOF material was characterized using various techniques, such as IR spectroscopy, PXRD, XPS, TGA, FESEM, and TEM, which revealed the successful formation of a heterostructure. Under sunlight, the photocatalyst effectively degraded two major organic pollutants methylene blue (MB) dye (~98%) and ciprofloxacin (CIP) antibiotic (~88%) *via* a multistep charge transfer mechanism. This process is primarily driven by solar energy, highlighting its potential for sustainable environmental remediation. Trapping experiments identified hydroxyl radicals ($^{\bullet}OH$) and superoxide radicals ($^{\bullet}O_2^-$) as the dominant reactive species in the degradation pathway. The degradation efficiency significantly increased with catalyst dosage, increasing from 72% to 98% for methylene blue (MB) as the dosage increased from 2.5 mg to 10 mg. Similarly, for ciprofloxacin (CIP), the efficiency improved from 53% to 88% when the catalyst dose was increased from 5 to 10 mg within 60 minutes. The photocatalyst exhibited excellent structural stability over 20 consecutive degradation cycles. Additionally, a detailed analysis of the degradation mechanism and kinetics studies provided valuable insights into the heterojunction design for developing high-performance magnetic photocatalysts for wastewater treatment. In alignment with the United Nations Sustainable Development Goal 6 (clean water and sanitation), this work addresses the urgent challenge of emerging organic pollutants in wastewater. Hence, this work highlights the potential of a sustainable and recyclable photocatalyst for wastewater treatment.

Received 19th December 2025
Accepted 10th February 2026

DOI: 10.1039/d5ra09822j

rsc.li/rsc-advances

Introduction

Wastewater generation and groundwater contamination are major environmental concerns today. Organic pollutants, like dyes and antibiotics, especially those used in the textile and pharmaceutical industries, can significantly impact the environment by contaminating water bodies. Methylene blue (MB), a common dye in textiles, can cause pollution,[1] can disrupt photosynthesis,[2] and can be toxic to marine life,[3] while ciprofloxacin (CIP), an antibiotic used in human and veterinary medicine, has a broad antimicrobial spectrum[4] that targets DNA gyrase[5] and topoisomerase IV[6] of various Gram-negative and Gram-positive bacteria, thus preventing cell replication.[7] It also poses challenges in water treatment due to its stability[8] and resistance to degradation.[9] The presence CIP contamination in water can indirectly affect human health and the environment, as it enters the food chain or requires energy-intensive processes to remove from water. Therefore, improving waste management and sustainable practices are crucial. Further, extracting organic pollutants and contaminants from water bodies has become a significant challenge, leading to the development of various wastewater treatment methods, including membrane filtration,[10] ozonation,[11] ion exchange,[12] adsorption,[13] catalytic reduction,[14] photocatalytic degradation,[15] and coagulation.[16] Among these, photodegradation processes, particularly photocatalysis, have gained popularity for pollutant elimination due to their high efficiency, simplicity, energy efficiency and environmental friendliness.

Photocatalysis, a type of heterogeneous catalysis, has emerged as a highly effective and time-efficient process that rapidly degrades organic pollutants under ambient conditions.[17] It facilitates the mineralisation of organic contaminants, breaking them down into harmless end products, like

[a]*Kalinga Institute of Industrial Technology (KIIT) Deemed to be University, Bhubaneswar 751024, India. E-mail: rsahufch@kiit.ac.in*

[b]*Department of Chemistry, NIST University, Institute Park, Berhampur 761008, India*

[c]*Energy Materials & Devices Division (EMDD), CSIR - Central Glass and Ceramic Research Institute, Raja S. C. Mullick Road, Jadavpur, Kolkata, 700032, India*

† Equal contributions.

water and carbon dioxide, without generating secondary pollutants. This aligns well with the goals of environmental remediation and wastewater treatment.[18] This method uses semiconductor photocatalysts to expedite chemical reactions, primarily focusing on the breakdown of environmental pollutants under sunlight or artificial light sources.[19] The effectiveness of photodegradation is significantly enhanced by the surface functionalization of nanomaterials. The efficiency of this degradation process depends on several operational parameters, such as the initial dye concentration, light intensity, reaction temperature, and pH of the solution. Furthermore, heterostructure photocatalysts have been widely adopted to enhance the photocatalytic activity of semiconductor materials, improve carrier utilization and facilitate the formation of effective radicals.[20]

In this context, metal organic frameworks (MOFs) are highly porous, crystalline materials composed of metal ion clusters connected by organic ligands, typically aromatic carboxylic acids or nitrogen-containing compounds.[21] These materials exhibit high surface areas and porosities, making them valuable in diverse applications, like catalysis,[22] sensing,[23] energy storage,[24] drug delivery,[25] and CO_2 capture.[26] Among the several subclasses of MOFs, zeolitic imidazolate frameworks (ZIFs), a specialized type of MOF, are garnering attention due to their extensive surface area, adjustable porosity, and robust thermal and chemical stability.[27] Structurally resembling zeolite molecular sieves, ZIF 67, are widely used in catalysis, adsorption, and separation.[28] However, challenges persist in the efficient recovery of ZIF 67 powder from aqueous solutions, limiting its utility in catalytic processes.

To overcome these limitations, the development and synthesis of magnetic nanocomposites are notable for their superior magnetic separation capabilities. $NiFe_2O_4$ (NF) nanoparticles are particularly interesting for photocatalysis due to their beneficial properties, including ferromagnetic nature,[29] low toxicity, high conductivity, and robust resistance to photon corrosion.[30] However, pristine NF has low photocatalytic efficiency due to several intrinsic factors. The high rate of recombination between photogenerated electrons and hole pairs limits the number of charge carriers available to participate in the redox process.[31] Moreover, NF typically has a lower surface area, leading to fewer active sites for photocatalytic reactions. Enhancements such as doping, composite formation, surface modification, and morphological control can improve the photocatalytic efficiency of NF.

Here, a magnetic composite catalyst, $NiFe_2O_4$@ZIF 67 (NFZ67), was developed by optimising the loading of NF in ZIF 67 to tackle water pollution. Previous studies predominantly rely on energy-intensive solvothermal or hydrothermal processes conducted at 120–200 °C, often requiring autoclave use, long reaction time and organic solvents, such as DMF and EG (ethylene glycol), which pose environmental concerns.[32] A detailed comparison of earlier syntheses of ferrite-based MOF hybrid materials is listed in Table S1 of the SI. In contrast, the present synthesis method of NFZ67 is performed using a green synthesis route in which a very low boiling solvent, that is methanol, is used at fully ambient temperature without any auxiliary template, mineralizers, surfactants, capping agents or reducing agent synthesis avoiding autoclave and eliminating the requirement for high thermal input, which reduces energy consumption, simplifies operation and enhances sustainability while maintaining the intrinsic porosity and crystallinity. Sunlight is crucial for driving photocatalytic reactions, making it cost-effective and eco-friendly. The composite was created by combining NF with ZIF 67 at ambient temperature. This method minimizes electron/hole pair recombination, making it an effective photocatalyst. This research focused on using NFZ67 composites to break down MB and CIP in an aqueous solution. Hence, the key novelty of our research lies in the green, room temperature synthesis of NFZ67, where the term "green" refers to low temperature and avoiding the use of harmful solvents, as reported.[34] The effectiveness of the composite was assessed by examining the impact of different catalysts and their concentrations. This study suggests that adsorption-mediated photodegradation is a promising solution for wastewater treatment because it efficiently and cleanly decomposes pollutants at room temperature without producing secondary contaminants and allows easy recovery of the photocatalyst from polluted water using an external bar magnet.

Experimental section

Materials and methods

Methylene blue (MB) dye and ciprofloxacin (CIP) were obtained from Merck. Cobalt nitrate hexahydrate [$Co(NO_3)_2 \cdot 6H_2O$], 2-methylimidazole ($C_4H_6N_2$, 2-MIM), nickel nitrate hexahydrate [$Ni(NO_3)_2 \cdot H_2O$], ferric nitrate hexanitrate [$Fe(NO_3)_3 \cdot 6H_2O$], methanol (MeOH), and sodium hydroxide (NaOH) were purchased from Merck Company (India). Distilled or DI water used was made in our laboratory. No further purifications are performed on the reagents before use.

Synthetic procedures

Synthesis of ZIF 67. ZIF 67 was synthesised using a previously reported method.[33] In an aqueous or methanolic metal solution of Co $(NO_3)_2 \cdot 6H_2O$, the linker 2-methylimidazole (Hmim) solution was added dropwise. The mixture solution was continuously stirred for 6 h at room temperature. Then, the resulting purple precipitates were collected by centrifugation (7000 rpm/10 min). The solid product was then washed three times with DI water, followed by washing with methanol. Finally, it was dried under vacuum at 80 °C for 24 h.

Synthesis of $NiFe_2O_4$. Using a simple hydrothermal synthesis technique, magnetic nickel ferrite was prepared.[34] The compounds Fe $(NO_3)_3 \cdot 9H_2O$ and Ni $(NO_3)_2 \cdot 6H_2O$ were solubilized in DI water while being subjected to magnetic agitation. To maintain pH 10, NaOH was added to the solution, and the solution was continuously stirred for 1 h. Thereafter, the resulting red-brown solution was transferred to an autoclave and heated at 180 °C for 18 h. After the autoclave cooled to room temperature, the resultant brown precipitate was extracted using an external bar magnet, subjected to three washing cycles with ethanol and distilled water, and subsequently dried at 70 °

C for 10 hours. The comprehensive scheme is illustrated in Fig. 1.

Green synthesis of the NFZ67 catalyst. A series of NFZ67 composites were synthesized using the above-mentioned procedure, with adjusted weight percentage of NF (10, 30, 50, and 70 wt% $NiFe_2O_4$ content based on the final product), and denoted as 10NFZ67, 30NFZ67, 50NFZ67, and 70NFZ67, respectively. Different amounts of NF were dispersed in 40 mL of aqueous or methanol and ultrasonicated. Then, Co $(NO_3)_2 \cdot 6H_2O$ was added to the above solution. In the next step, 2-methylimidazole (Hmim) with 40 mL of methanol solution was added dropwise to the above solution. The final solution was stirred at room temperature for 6 h and kept overnight to settle down. The product was separated using a centrifuge at 7000 rpm for 10 min, washed 3 times with methanol, and dried at 80 °C for 12 h.

Evaluation of photocatalytic performance. The photocatalytic activity of the synthesized catalysts (ZIF 67, NF, and NFZ67) was assessed under natural sunlight. For the experiments, varying amounts of each catalyst were dispersed in 25 mL of MB solution (30 ppm) and CIP solution (10 ppm). Before light exposure, the suspensions were stirred in the dark to establish an adsorption–desorption equilibrium. Following this, the solutions were irradiated with sunlight to initiate the photodegradation process. At specific time intervals, the samples were withdrawn, and the catalyst was separated using an external bar magnet. The concentrations of MB and CIP in the resulting supernatants were analysed using a UV-Vis spectrophotometer over the wavelength range of 200–800 nm. Photodegradation experiments conducted without any catalyst are taken as the control. A slight reduction in MB and CIP concentrations was observed in the control due to direct sunlight exposure and the nature of the peaks, as shown in Fig. 6. However, the NFZ67 composite demonstrated superior performance, achieving degradation efficiencies of approximately 98% for MB and 88% for CIP within 60 minutes.

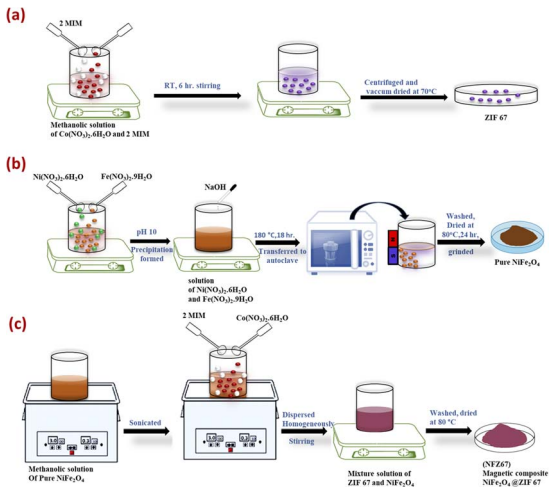

Fig. 1 Schematic of the catalyst synthesis: (a) ZIF 67, (b) NF and (c) NFZ67.

Additionally, to determine the optimal pH for degradation, pH adjustments were made using NaOH and HCl.

The photocatalytic efficiency of the pollutant was evaluated using eqn (1):

$$\%\ \text{Degradation} = \frac{C_0 - C}{C_0} \times 100 \quad (1)$$

where C_0 and C are concentrations at the initial time and the given time interval of the pollutant, respectively.

Furthermore, 30NFZ67 composites were subjected to repeated reaction cycles to evaluate their recyclability. Following each cycle, the photocatalyst was retrieved, thoroughly washed using DI water and ethanol and dried at 348 K prior to being reused in the next test.

Results and discussion

Cobalt-based ZIF 67 is synthesized through a green synthesis technique at room temperature in a methanolic solution. Then, NF is combined to generate magneto NFZ67 catalysts. PXRD was executed to identify the crystallographic information and symmetry of the synthesized materials (Scheme 1).

The PXRD patterns of ZIF 67, NF and the NFZ67 composites are shown in Fig. 2(a). The main diffraction peaks of the synthesized ZIF 67 at 2θ values of 7.1°, 10.4°, 12.7°, 14.8°, 16.5°, 18.4°, and 22.1° corresponded to the (011), (002), (112), (022), (013), (222), and (114) reflections of ZIF 67, respectively, which well matches the reported data.[33] The PXRD pattern of pure $NiFe_2O_4$ displays characteristic peaks at 2θ angles of 30.41°, 35.68°, 43.26°, 53.89°, 57.37°, 62.91°, and 74.05° indexed to the (220), (311), (400), (422), (511), (400), and (533) crystallographic planes, respectively. These reflections confirm the formation of a cubic spinel structure typical of $NiFe_2O_4$.[34,35] The 30NFZ67 composite contains sharp peaks of both ZIF 67 and NF, and the peak position does not shift, which confirms the formation of the composite and the retention of both crystal structures. No extra peaks in the system indicate the high purity of the final NFZ67 composite. The PXRD pattern of all the prepared materials is mentioned to verify the phase consistency even after composite formation (Fig. S1).

FTIR spectroscopy was utilised to identify the functional groups existing in the material within the spectral range of 4000–500 cm^{-1} [Fig. 2(b)]. The peaks at 3127 and 2923 cm^{-1} are attributed to C–H stretching vibrations originating from both the aromatic ring and the aliphatic chain in H-MIM. Peaks found in the range of 1550–1350 cm^{-1} and 1578 cm^{-1} are

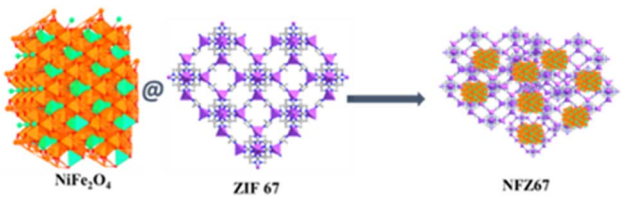

Scheme 1 Schematic representation for NFZ67 composites.

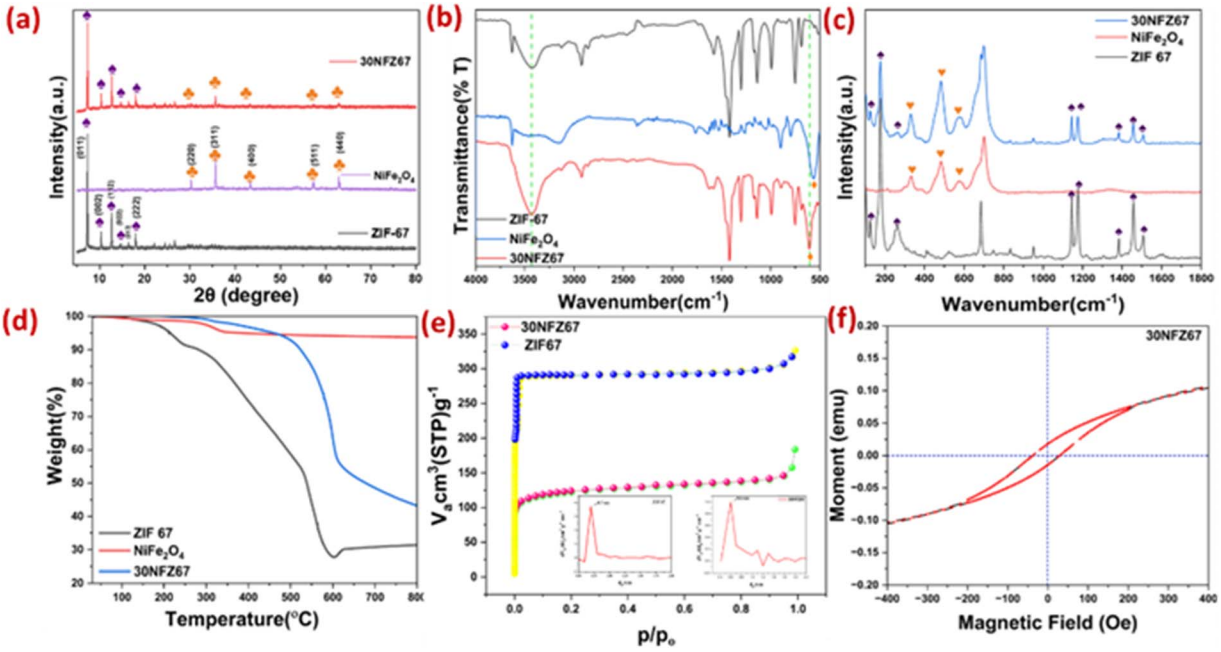

Fig. 2 (a) PXRD pattern, (b) FTIR spectra, (c) Raman spectra, (d) TGA curves, (e) BET curves: insets: the pore diameter of ZIF 67 and 30NFZ67, and (f) VSM graph of the catalysts.

associated with ring vibrations and stretching vibrations of C=N, respectively. The spectral region between 1300 and 991 cm^{-1} displays various bands linked to the in-plane bending vibrations of the imidazole ring. A characteristic peak at 752 cm^{-1} corresponds to Co–N stretching. Additionally, peaks at 1137.4 cm^{-1} and 1417 cm^{-1} correspond to C–N bending and C=C stretching, respectively. The FTIR spectrum of synthesized ZIF 67 well matched the reported data.[33,36] In the $NiFe_2O_4$ spectrum, a prominent absorption band observed at 555 cm^{-1} corresponds to the Fe–O–Fe stretching vibration.[34] The peak position of 30NFZ67 significantly changes from 555 to 603 cm^{-1}, as observed in $NiFe_2O_4$, indicating the formation of a new composite material, *i.e.* NFZ67, which is chemically bonded.[37] The surface of 30NFZ67 contains the characteristic signal of ZIF 67 and $NiFe_2O_4$, indicating the effective synthesis of the composite.

The vibrational modes of ZIF 67, NF, and the 30NFZ67 composite were examined. Specific peaks at 176 cm^{-1}, 685 cm^{-1}, 1146 cm^{-1}, and 1457 cm^{-1} were linked to Co–N stretching, Imidazole ring puckering, C–N stretching, and methyl bending modes of ZIF 67, respectively.[38] NF exhibited peaks at approximately 331 cm^{-1}, 482 cm^{-1}, 574 cm^{-1} and 702 cm^{-1}, with an additional shoulder around 660 cm^{-1}, 331 cm^{-1} and 660 cm^{-1} representing the E_g modes, while 482 cm^{-1} represents T_{2g}, 574 cm^{-1} and 702 cm^{-1} represents A_{1g} vibrational modes.[39] All Raman spectra displayed peaks related to NF [Fig. 2(c)]. In the 30NFZ67 composite, all these peaks were present. Notably, peaks in the 600–700 cm^{-1} range slightly broadened, forming a doublet, which indicated chemical interactions between ZIF 67 and NF. The intensities of the composite decreased because NF was loaded into ZIF 67, demonstrating that this composite is not merely a physical mixture but involves chemical interactions. The thermal behaviour of ZIF 67, NF, and NFZ67 was analysed using TGA [Fig. 2(d)]. In ZIF 67, the 1st weight loss occurred between 190 °C and 290 °C due to the decomposition of unreacted species. The 2nd weight loss is due to the decomposition of the imidazole linker in temperature range of 300–510 °C. The thermal decomposition of NF takes place in three stages at temperature ranges of 30–100 °C, 100–350 °C, and 350–600 °C. The first decomposition is due to the breakdown of the NF complex and evaporation of H_2O molecules, the 2nd weight loss is due to the continuing oxidation of organic matters, and the decomposition of inorganic salts and the 3rd weight loss may be due to the formation of metal oxides. At temp. above 630 °C, there is no weight loss observed.[40] From the TG curve of the composite, it is clearly observed that 30NFZ67 is highly stable up to 610 °C, and there is no major weight loss in between. A detailed peak analysis is depicted in Fig. S2.

As most catalytic reactions occur on the surface of the catalyst, the catalyst's surface area becomes a crucial factor. Fig. 2(e) displays the nitrogen gas sorption isotherms of pure ZIF 67 and 30NFZ67. The BET surface areas of ZIF 67 and 30NFZ67 are determined to be 1143 $m^2 g^{-1}$ and 581.2 $m^2 g^{-1}$, respectively. The introduction of NF into ZIF 67 leads to a decrease in surface area, which is attributed to pore blockage and changes in structure. Although this may seem initially disadvantageous, it serves a strategic purpose in applications related to dye and antibiotic degradation. NF, located within the highly porous framework of ZIF 67, acts as a carrier that enhances the catalytic properties of the composite. This enhancement occurs through the interaction of NF with pollutant molecules, thereby facilitating a more effective degradation process compared to using ZIF 67 alone. Despite the reduction in total surface area, the

composite benefits from synergistic effects where NF's catalytic function complements the adsorptive capabilities of ZIF 67. This synergy results in improved efficiency in breaking down intricate pollutant molecules during the treatment of wastewater, positioning the 30NFZ67 composite as a valuable resource in environmental remediation efforts where efficient pollutant degradation holds significance. The pore size distribution graph indicates that both ZIF 67 and 30NFZ67 contain micropores with pore volumes of 0.7 nm and 0.6 nm, respectively. Therefore, the presence of magnetic nanoparticles in the catalyst can enhance electron transfer processes, which can lead to improved catalytic activity and faster degradation rates compared to non-magnetic catalysts. The magnetic properties of NF and 30NFZ67 were measured at room temperature [Fig. 2(f)]. The VSM data of 30NFZ67 reveal that the composite material is superparamagnetic with negligible coercivity and remanence. Due to the introduction of non-magnetic ZIF 67 into NF, the saturation magnetisation (M_s) value of 30NFZ67 is lower compared to pure NF (Fig. S6). The reduction in the magnetization of NFZ67 is primarily attributed to the lower concentration of magnetic nanoparticles and the presence of crystalline ZIF 67. Nevertheless, M_s of 30NFZ67 is still sufficient to collect the catalyst from the pollutant solution. The magnetic nature of 30NFZ67 enables easy separation and recovery from the solution using an external bar magnet, thereby facilitating catalyst reuse while reducing operational costs and waste generation.

To examine the light harvesting nature of magnetic NFZ67, UV DRS spectra were recorded and the optical bandgap (E_g) was calculated. Fig. 3(a) represents the UV DRS spectra of ZIF 67, NF and 30NFZ67 composite, and each peak notably showed strong absorption in the UV-Vis range, with ZIF 67 displaying a distinct absorption band from 450 nm to 600 nm. The peaks at 590 and 258 nm are attributed to $^4A_2(F) \rightarrow {}^4T_1(P)$ of Co^{2+} ions and ligand to metal charge transfer (LMCT) transition, respectively.[38] These results indicate that ZIF 67 has the majority of tetrahedrally coordinated Co^{2+} on its structure.[41] NF is considered to be an indirect band gap material because phonons are involved in the optical absorption process.[39] The bandgaps of ZIF 67, NF and NFZ67 are calculated as 1.83 eV, 1.55 eV and 1.49 eV, respectively, using Tauc plot [Fig. 3(b)]. The lower E_g value of the samples is helpful for enhancing light absorption and photocatalytic efficiency. The 30NFZ67 exhibited broader and more intense light absorption in the visible spectrum, suggesting that ZIF 67 significantly contributed to improving the materials light harvesting nature, with wider and stronger adsorption intensity in the visible region. The effectiveness of separating charges plays a pivotal role in determining the efficacy of photocatalysts. In order to scrutinize the behaviour of electron (e^-) and hole (h^+) pairs generated by light. The PL peak of 30NFZ67 noticeably diminishes as we load the NF in the composites, signalling effective charge separation within the composites. The outcome illustrates NF's effective suppression of recombining photoinduced e^- and h^+ pairs in ZIF 67, thereby extending the lifespan of e^-/h^+ pairs and enhancing charge transfer at the interface.

Fig. 4 presents the X-ray photoelectron spectra of each element from which the detailed chemical composition can be studied. ZIF 67 contains Co and N; NF contains Ni, Fe, and O; and 30NFZ67 contains Co, Ni, Fe, and O. In ZIF 67, Co has two signature peaks around 781.1 eV and 797.1 eV, which are mainly attributed to Co $2p_{3/2}$ and Co $2p_{1/2}$, respectively, while 786.8 eV and 802.8 eV are satellite peaks. In NF, the Ni 2p spectra display prominent peaks at 856 eV and 873.6 eV corresponding to Ni $2p_{3/2}$ and Ni $2p_{1/2}$ with satellite peaks observed at 862.2 and

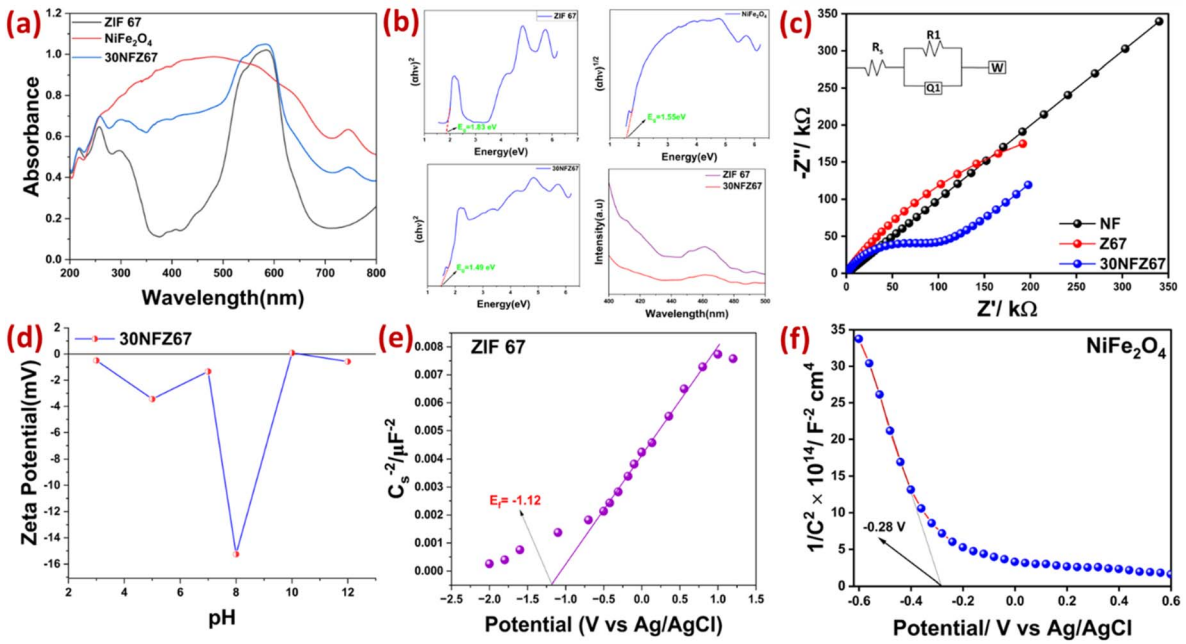

Fig. 3 (a) UV DRS spectra, (b) TAUC plots and PL spectra, (c) impedance plots: inset: the appropriate equivalent electrical circuit, (d) zeta potential graph and Mott Schottky plots of (e) ZIF 67, (f) NF.

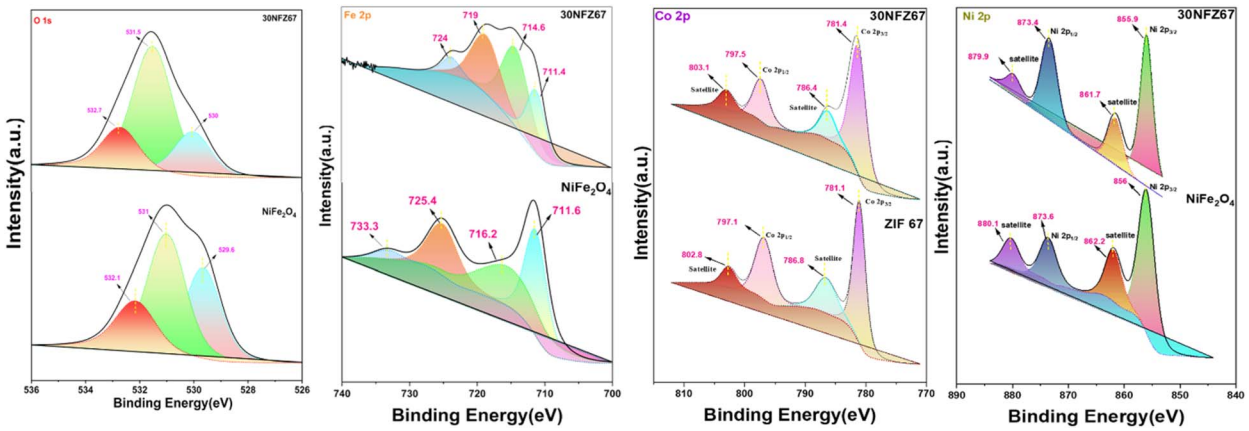

Fig. 4 XPS spectra of O 1s, Fe 2p, Co 2p, and Ni 2p in ZIF 67, NF and 30NFZ67.

880.1 eV, respectively. For the Fe 2p region, distinct peaks are found to be at 725.4 eV and 711.6 eV for Fe $2p_{1/2}$ and Fe $2p_{3/2}$, respectively, along with satellite peaks around 716.2 eV and 733.3 eV. For O 1s, there are three peaks at 529.6, 531, and 532.1 eV, indicating lattice oxygen, oxygen vacancy and surface adsorbed oxygen, respectively.[42] The XPS spectra of the composite show characteristic peaks of both ZIF 67 and 30NFZ67 with noticeable shifts in binding energy compared to the pristine materials. This shift confirms the electronic interaction between the two components. The coexistence of Co^{2+} and Ni^{2+} oxidation states and their respective satellite features indicates the successful formation of the 30NFZ67 composite without altering the core chemical states, thereby proving composite formation. The full XPS spectra are shown in Fig. S5.

The surface morphology and structural characteristics of ZIF 67, NF, and 30NFZ67 composite were analysed using FESEM and TEM. As illustrated in Fig. 5(a–c), the SEM images reveal that ZIF 67 exhibits a well-defined rhombic dodecahedral structure with an average particle size of approximately 350 nm. In contrast, NF particles appear irregular in shape likely due to particle agglomeration caused by strong magnetic interactions. FESEM images of the 30NFZ67 composite at various magnifications indicate a uniform distribution of NF on the surfaces of the ZIF 67 crystals, confirming the successful synthesis of the composite material. Elemental mapping of 30NFZ67, presented in Fig. S4, shows the presence of all characteristic elements of both pristine ZIF 67 and NF, further validating the formation of the composite. Moreover, TEM analysis offers deeper insight into the morphology and the interface between NF and ZIF 67, providing clear evidence of heterojunction formation (30NFZ67). The images distinctly demonstrate that the magnetic NF is anchored to the ZIF 67 surfaces, aligning well with the observations made from the FESEM analysis. The ZIF 67 surfaces were successfully compounded and consistent with the results of the SEM images.

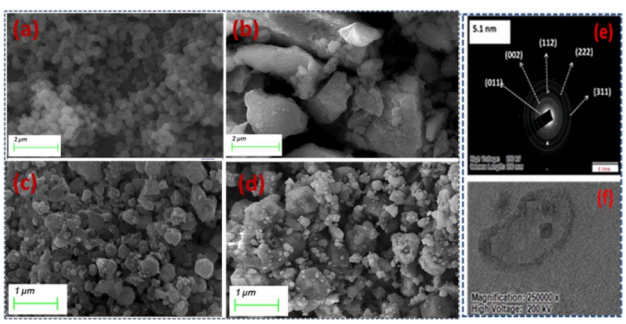

Fig. 5 FESEM images of (a) ZIF 67, (b) NF, (c and d) 30NFZ67, and (e and f) TEM images of the 30NFZ67 composites.

Photocatalytic degradation

Considering the characterization, such as photophysical properties, surface area and morphology, we used 30NFZ67 in photocatalytic activity. MB and CIP were selected as representative degradation compounds under sunlight to evaluate the photocatalytic efficiency of NFZ67, with each experiment repeated three times. The degradation efficiency was evaluated by optimizing various parameters, like the effect of different NF content, catalytic dose, pH, and pollutant concentration. In order to conduct the experiment, both the pollutant solutions were exposed to light without any catalyst, and no major changes in absorbance were observed. Then, to investigate the efficiency of NFZ67, we added different amounts of the catalyst to 30 ppm and 10 ppm of MB and CIP solutions, respectively, and the solutions were kept in dark until it reached equilibrium. Then, the solutions were exposed to light for 90 min. A significant decrease in absorbance and an increase in removal efficiency were observed, as shown in Fig. 6. The visual representation of the MB solution before and after degradation over time is depicted in Fig. S8. As CIP is colorless, no picture is given.

The effects of various catalysts, *i.e.*, ZIF 67, NF, 10NFZ67, 30NFZ67, 50NFZ67, and 70NFZ67, on the photocatalytic degradation of MB and CIP were systematically studied. All the composite catalysts exhibited improved degradation efficiency compared to ZIF 67 and NF, indicating the synergistic effect and significance of the composite structure.

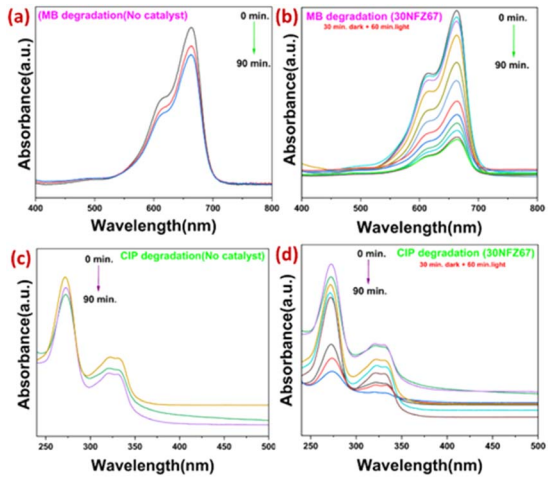

Fig. 6 Degradation of MB and CIP (a and c) without a catalyst and (b and d) with a catalyst.

As shown in Fig. 7(a), increasing the $NiFe_2O_4$ content from 10% to 30% in the NFZ67 composites led to a notable enhancement in degradation efficiency. However, low removal efficiency was observed in the cases of 50NFZ67 and 70NFZ67. Among all the catalysts, the 30NFZ67 composite exhibited the highest activity for the degradation of both MB and CIP. 30NFZ67 degrades ~98% of MB and ~88% of CIP in 60 min. To realize the completion of the degradation process, the experiment continued until 90 min; the observation revealed that there are no further changes in the last 30 min of the photo irradiation. Hence, the optimized time was taken as 60 min. These enhanced results may be attributed to the suitable incorporation of NF into the composite structure, which increases the number of active sites and thus absorbs more pollutants. However, when the NF content increases, it tends to agglomerate on the ZIF 67 surface and lowers the number of exposed active sites, potentially hindering the transfer of photogenerated charges across the interfaces, which is not conducive to further increasing the photodegradation efficiency. In order to study the effect of catalyst dose on the degradation of MB and CIP, a systematic exploration was undertaken by varying the dosage from 2.5 mg to 20 mg. All dosages have a good degradation efficiency, with the highest degradation rate of ~98% for MB and ~88% for CIP. Kinetic studies of MB and CIP degradation using 30NFZ67 composites provide key insights into catalytic efficiency and reaction pathways. The photodegradation of both MB and CIP follows pseudo-first-order kinetics using the following equation, with apparent rate constants $k = 0.03852\ \text{min}^{-1}$ and $k = 0.02097\ \text{min}^{-1}$ for MB and CIP, respectively:

$$-\ln(C/C_0) = kt$$

where C_0 and C are the initial and instantaneous concentrations of organic pollutant at time t, respectively, k is the apparent rate constant (min^{-1}) and t is the irradiation time.

In comparison, pristine ZIF-67 exhibits lower rate constants of $k = 0.00588\ \text{min}^{-1}$ and $k = 0.01405\ \text{min}^{-1}$ for MB and CIP, respectively, highlighting the enhanced photocatalytic performance of the 30NFZ67 nanocomposites. The degradation efficiency of MB increased from 72% to 98% and the rate constant increased from $0.00588\ \text{min}^{-1}$ to $0.03852\ \text{min}^{-1}$ as the catalyst dosage increased from 2.5 mg to 10 mg in 60 min; for CIP, the rate constant increased from $0.01405\ \text{min}^{-1}$ to $0.03585\ \text{min}^{-1}$

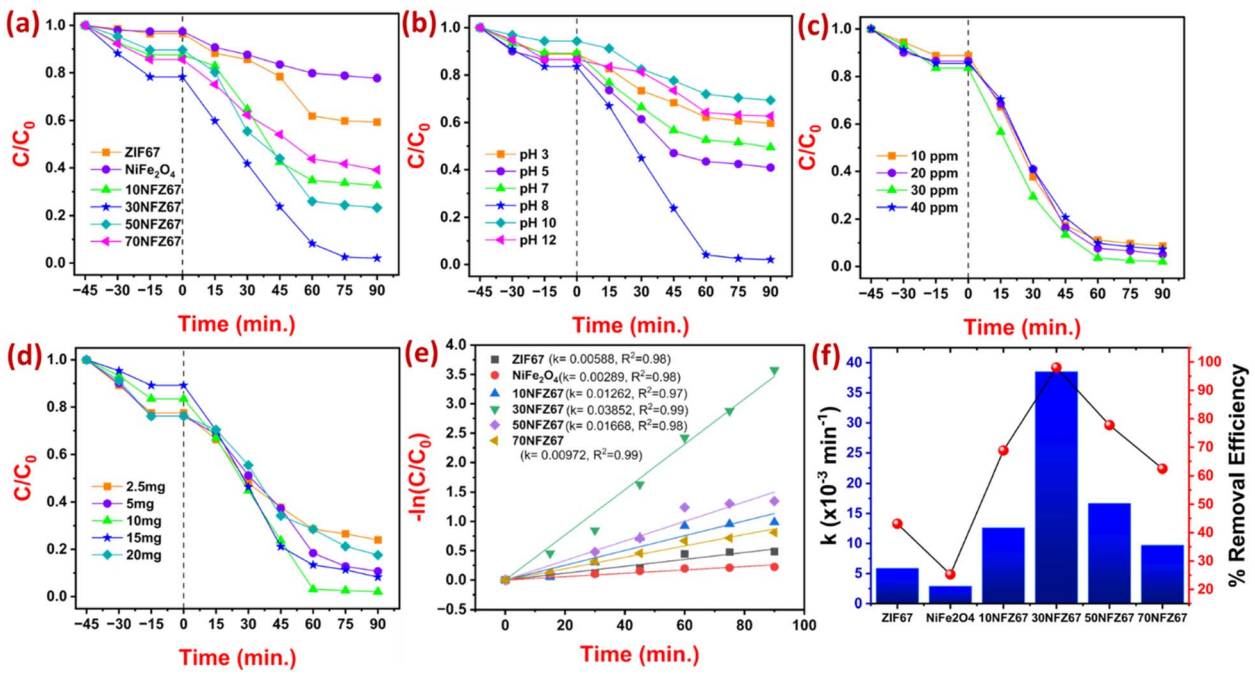

Fig. 7 Effect of different parameters on the removal efficiency of MB: (a) different catalyst , (b) catalyst dose, (c) pH, (d) dye concentration, (e) pseudo-first-order kinetic fitting and (f) rate constant.

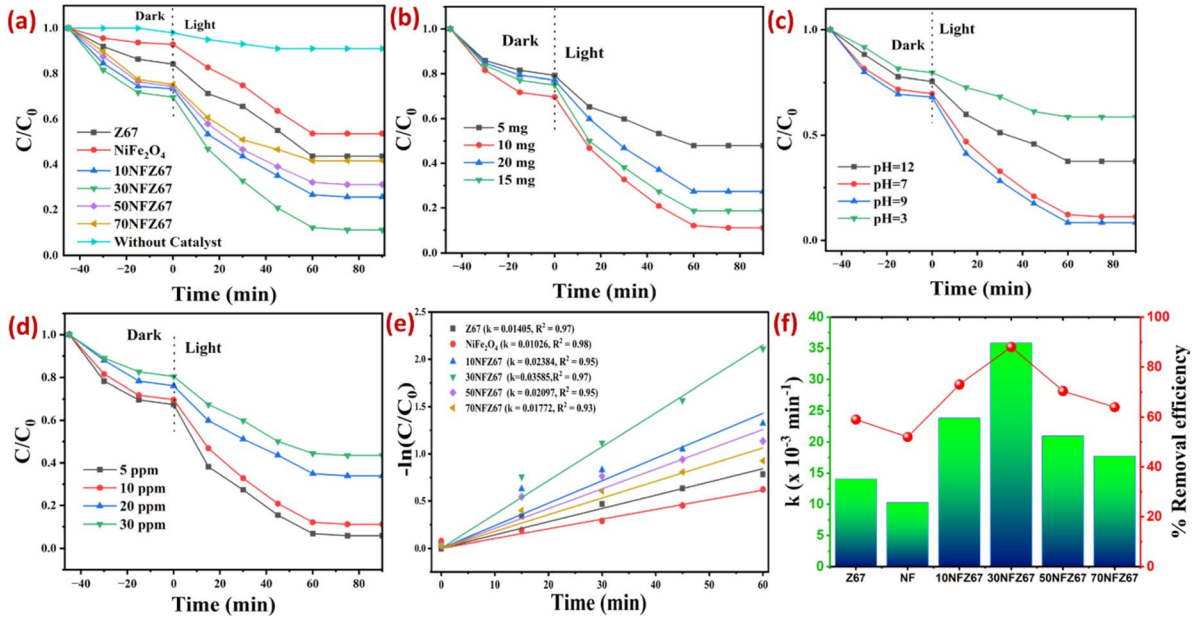

Fig. 8 Effect of different parameters on the removal efficiency of CIP: (a) different catalyst, (b) catalyst dose, (c) pH, (d) antibiotic concentration, (e) kinetic fitting and (f) rate constant.

(Fig. 8). The reasons may be that more catalysts would provide more active sites to react with pollutants, which enhances the formation of $^{\bullet}OH$ and promotes pollutant breakdown. However, with the further increasing dosage from 10 mg to 20 mg, the efficiency decreases slightly. This effect may be due to excessive catalysts hindering light penetration, thereby limiting photon absorption. Other reasons may be attributed to both the aggregation and sedimentation of 30NFZ67, which reduces the number of available active sites. Based on the cost and effectiveness of photodegradation, a catalyst dosage of 10 mg was selected as the optimal amount for the experiments.

The effect of the initial pollutant concentration is very important for the practical usage of the photocatalyst. As shown in Fig. 7(d), the degradation efficiency of MB and CIP increased as the initial concentration increased from 5 ppm to 30 ppm and decreased when it reached 40 ppm. This enhanced efficiency may be due to a decrease in the recombination of charge carriers at the surface of 30NFZ67. The reduction in efficiency is likely due to the higher concentration of pollutant molecules adsorbed on the catalyst surface, which hinders light from directly interacting with the catalyst. Hence, the amounts of reactive radicals produced on the surface of the catalyst decrease relatively.

To confirm the surface charge characteristics of the 30NFZ67 catalyst, zeta potential measurements were conducted. The zeta potential reflects the electrical potential of particles in a suspension and serves as an indicator of colloidal stability. As illustrated in Fig. 3(d), the zeta potential of 30NFZ67 varies with pH, showing a transition from negative to positive values. The isoelectric point, where the zeta potential equals zero, occurs at approximately pH 10.5. Under acidic conditions (pH < 7), the catalyst surface carries a negative charge. Notably, at pH 8, the zeta potential reaches around −16 mV, indicating a pronounced negative surface charge. This may be attributed to the deprotonation of surface functional groups or the adsorption of negatively charged species. As the pH increases beyond 8, the zeta potential gradually becomes less negative, eventually reaching zero at pH 10.5. This shift marks the point of zero charge for the catalyst. The pH of the solution plays a crucial role in influencing the photocatalytic degradation process, as it affects both the surface charge of the catalyst and the ionization state of the target pollutants. These factors directly impact the interactions between the catalyst and the adsorbates, such as MB and CIP. To investigate the influence of pH on degradation efficiency, a series of experiments were performed across a range of pH values. The results demonstrated that at lower pH levels, the catalyst surface was negatively charged. As the pH increases from 3 to 9, there is a noticeable improvement in the adsorption of MB and CIP. This enhancement can be attributed to a reduction in positive surface charge, which favors electrostatic attraction between the negatively charged pollutants and the catalyst surface, thus promoting more effective degradation. These findings are consistent with the trends observed in the zeta potential data.

To explore the reasons for the rapid degradation efficiency of 30NFZ67, impedance tests were conducted, as shown in [Fig. 3(c)]. The Nyquist plot reveals the impedance behaviour of NF, Z67, and 30NFZ67, where the semicircle size corresponds to the charge transfer resistance (R_{ct}). Among the samples, 30NFZ67 exhibits the smallest semicircle, indicating the lowest R_{ct} and the most efficient charge transfer. This reduced impedance enhances electron transport and minimizes recombination of electron–hole pairs, which are crucial for photocatalytic processes. The superior performance of 30NFZ67

can be attributed to its improved electronic properties, structural modifications, and potential synergistic effects that enhance active sites and facilitate pollutant adsorption. These properties collectively result in better interfacial charge transport, making 30NFZ67 the most effective for degradation.

Possible mechanism and degradation pathway

The mechanism of MB and CIP degradation using the 30NFZ67 semiconductor is illustrated in Fig. 9. This process follows a series of step reactions, beginning with photoexcitation. In the photocatalytic degradation process using semiconductor materials, superoxide radicals ($O_2^{\bullet -}$) and hydroxyl radicals ($OH^{\bullet}$) play critical roles. When sunlight irradiates the polluted solution, photoelectrons (e^-) within the 30NFZ67 semiconductor become excited. When the photocatalyst absorbs photons with energy ($h\nu$) equal to or greater than the semiconductor's bandgap, electrons from the valence band (VB) are excited and move to the conduction band (CB), leaving behind a hole (h^+) in VB. This process results in the generation of an electron–hole pair (e^-/h^+), as shown in the equation below.

The flat-band potential (E_f) and semiconductor types of the materials were determined using a Mott–Schottky (MS) analysis. The positive slope observed for ZIF 67 indicates that it is an n-type semiconductor, while the negative slope for $NiFe_2O_4$ confirms its p-type nature. The E_f values referenced against the Ag/AgCl electrode were found to be −1.12 V for ZIF 67 and −0.28 V for $NiFe_2O_4$. These were adjusted to the normal hydrogen electrode (NHE) scale using the following formula:

$$E_{NHE} = E_{Ag/AgCl} + 0.198\ V + 0.0592 \times pH$$

The calculated E_{CB} values for NF and ZIF 67 are −1.21 eV and −0.57 eV and E_{VB} values are 0.332 eV and 1.26 eV, respectively, with reference to the normal hydrogen electrode at pH 6.9, calculated using the following equation:

$$E_{VB} = E_{CB} + E_g$$

where E_g = band gap energy, E_{CB} = conduction band edge potential, and E_{VB} = valence band edge potential.

For superoxide anion radicals to form, the CB must have a more negative potential than the oxygen reduction potential (−0.33 V). In contrast, the generation of hydroxyl radicals requires the VB to possess a more positive potential than the water oxidation potential (1.99 V). The photocatalytic activity of the $NiFe_2O_4$/ZIF 67 heterojunction system can be explained based on its favourable band edge alignment and synergistic charge transfer mechanism. The more negative E_{CB} of $NiFe_2O_4$ facilitates photoinduced electron transfer to the less negative E_{CB} of ZIF 67 *via* the Ni–Fe–O–Co heterojunction. ZIF 67, known for its excellent electrical conductivity and electron affinity, acts as an efficient electron acceptor and transport medium, suppressing charge recombination. In the 30NFZ67 heterostructure, NF transferred electrons to the conduction band of ZIF 67 due to the difference in Fermi energy level and the electrons in the E_{CB} of Z67 interact with molecular oxygen, leading to the formation of superoxide radicals ($^{\bullet}O_2^-$), whereas the holes present in the valence band facilitate the oxidation of water molecules or hydroxide ions adsorbed on the surface, resulting in the generation of hydroxyl radicals ($^{\bullet}OH$). The photogenerated holes in the VB (h_{VB}^+) of ZIF 67 react with surface-bound water or hydroxide ions (OH^-) to produce hydroxyl radicals ($OH^{\bullet}$). These OH radicals, formed on the irradiated semiconductor surface, are highly potent oxidizing agents. The persistent generation of $^{\bullet}O_2^-$ from the reduction of O_2 by CB electrons further contributes to the oxidative degradation process. Hence, the reduced recombination rate can be attributed to a multistep energy transfer process that enhances photocatalytic performance under sunlight exposure.

$$NiFe_2O_4/ZIF67 + \text{photons } (h\nu) \rightarrow e_{CB}^- + h_{VB}^+$$

$$e_{CB}^- + O_2 \rightarrow O_2^{\bullet -}$$

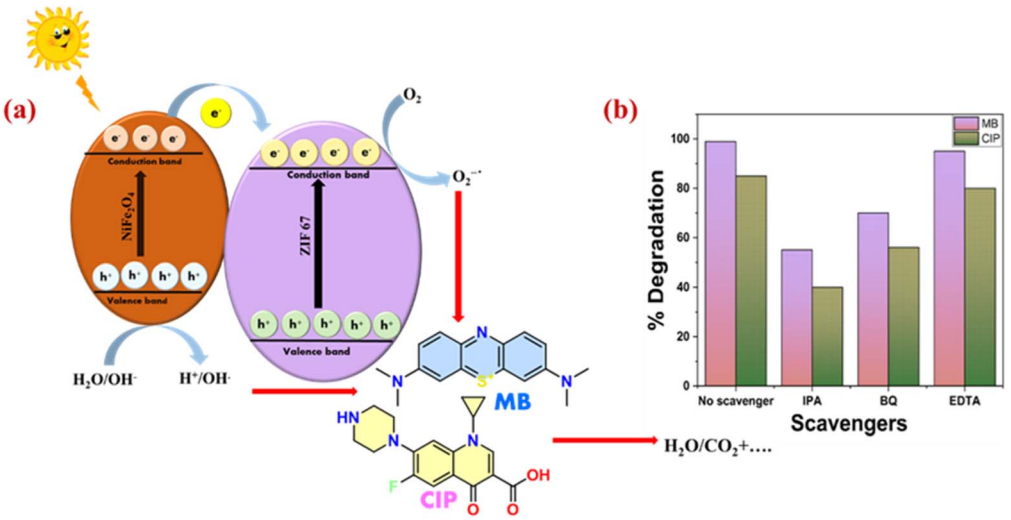

Fig. 9 (a) Plausible multistep electron transfer mechanism and (b) trapping experiments.

$$h_{VB}^{+} + H_2O \rightarrow H^+ + OH^- \rightarrow O\dot{H}$$

$$MB + OH^{\bullet} + O_2^{\bullet -} \rightarrow CO_2 + \cdots MB + OH^{\bullet} + O_2^{\bullet -}$$

$$CIP + OH^{\bullet} + O_2^{\bullet -} \rightarrow \text{Oxidative ring cleavage + non toxic products} + \cdots CIP + OH^{\bullet} + O_2^{\bullet -}$$

This dual-radical mechanism not only ensures the efficient degradation of dyes and antibiotics but also maintains charge neutrality by preventing electron–hole recombination through a phenomenon known as oxygen ionosorption.

The generated superoxide radicals ($O_2^{\bullet -}$) undergo protonation to form hydroperoxyl radicals ($HO_2^{\cdot}$), which subsequently convert to hydrogen peroxide (H_2O_2). Here, H_2O_2 subsequently breaks down into highly reactive hydroxyl radicals ($OH^{\bullet}$). These redox reactions generally take place on the surface of the semiconductor photocatalyst when it is activated by light, facilitating the degradation of pollutants. The degradation pathways of MB and CIP are illustrated in Fig. 10. In the case of MB, several major intermediates were identified, reflecting the breakdown of the parent dye molecule using LC-MS (Fig. S7). A degradation product with $m/z = 270.19$ corresponds to Azure B, which is formed *via* the primary oxidative *N*-demethylation of methylene blue. Another intermediate with $m/z = 284.21$ is identified as hydroxy-methylene blue, resulting from the electrophilic attack of hydroxyl radicals ($^{\bullet}OH$) on the electron-rich aromatic ring of MB, typically at *para*- or *ortho*-positions. Additionally, a fragment with $m/z = 135.16$ corresponds to *N*,*N*-dimethylaniline, which is formed by cleavage of the aromatic amine group. Similarly, the degradation of CIP ($m/z = 332$) involves several oxidative and structural transformation steps. The product with $m/z = 135$ indicates cleavage of the quinolone ring, yielding a fluoro-substituted aniline derivative. A compound with $m/z = 176$ is attributed to ring scission, leading to a hydroxymethyl-substituted aromatic structure. The intermediate with $m/z = 269$ suggests hydroxylation and ring opening of the piperazine ring, which is accompanied by the formation of carboxylic acid groups, while the product at $m/z = 376$ indicates that the piperazine ring is oxidized to an open-chain structure, while the core quinolone and cyclopropyl groups are retained.

In order to confirm and identify all the active reactive oxygen species (hydroxyl radicals, superoxide radicals, or holes) responsible for the degradation of pollutants, a trapping experiment was conducted. For this, 30 ppm MB dye and 10 ppm CIP solution were placed in a beaker, and 10 mg of photocatalyst was dispersed in the solution to form a suspension. A control experiment was set up without any trapping agents to establish the baseline degradation efficiency, and the MB concentration was periodically measured using a UV-Vis spectrophotometer. Individual trapping experiments were carried out using different scavengers. 10 mM isopropanol for hydroxyl radicals ($OH^{\bullet}$), 1 mM *p*-benzoquinone for superoxide radicals ($O_2^{\bullet -}$), and 1 mM EDTA to capture photogenerated holes (h^+). These mixtures are exposed to sunlight, and the MB and CIP concentrations are periodically measured. The degradation rates of MB and CIP in the presence of different trapping agents are compared with those of the control experiment, and the detailed data are presented in Fig. 9. A significant decrease in the degradation rate with a specific trapping agent indicates the involvement of the corresponding reactive species. Isopropanol is used to quench hydroxyl radicals ($^{\bullet}OH$) due to its high reactivity through hydrogen abstraction, which reduces $^{\bullet}OH$ availability. *p*-Benzoquinone selectively traps superoxide radicals ($^{\bullet}O_2^-$) by accepting electrons to form semiquinone radicals, thereby indicating the role of $^{\bullet}O_2^-$ in the reaction. EDTA serves as an effective hole (h^+) scavenger by donating electrons, preventing holes from participating in oxidation reactions.

$$^{\bullet}OH + (CH_3)_2CHOH \rightarrow H_2O + (CH_3)_2C^{\bullet}OH$$

$$^{\bullet}O_2^- + BQ \rightarrow BQ^{\bullet -} + O_2$$

$$h^+ + EDTA \rightarrow EDTA^+$$

A significant drop in methylene blue degradation upon the addition of these agents helps confirm the involvement of these reactive species in the photocatalytic mechanism. The analysis shows that hydroxyl radicals play a significant role when degradation decreases in the presence of isopropanol, superoxide radicals are important when *p*-benzoquinone reduces degradation, and holes are actively involved when degradation decreases with EDTA. Thus, $^{\bullet}OH$ has a more significant impact than other ROS.

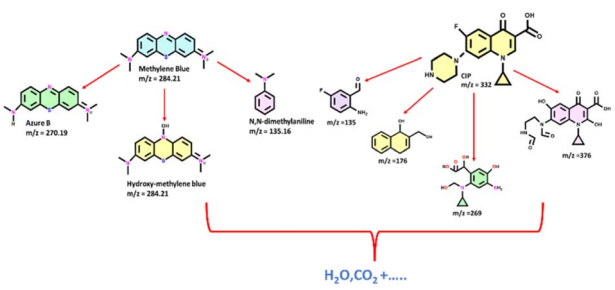

Fig. 10 Possible degradation pathways of MB and CIP.

Regeneration and reusability of the photocatalyst

The durability and recyclability of the 30NFZ67 catalyst were evaluated through multiple use cycles. Following each batch reaction, the 30NFZ67 catalyst was separated using a bar magnet, rinsed three times with water and ethanol, and then dried at 50 °C for reuse. The results, illustrated in Fig. 11, demonstrate that the photocatalytic efficiency of 30NFZ67 remains largely consistent over twenty successive cycles under sunlight. A slight 6–7% decrease in degradation efficiency in the 20th cycle proves the excellent stability of our catalyst, which is more than the current state of the art. The decrease in efficiency may be attributed to the loss of the catalyst during the washing and leaching of the material. Overall, this study highlights its

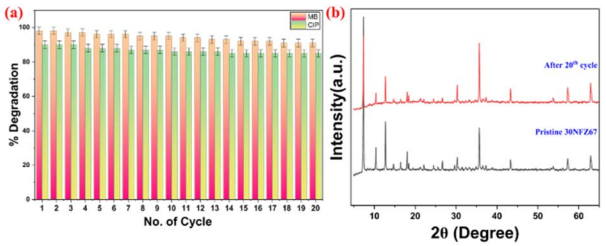

Fig. 11 (a) Recyclability of the catalyst 30NFZ67 for the photodegradation of MB and CIP and (b) PXRD pattern of 30NFZ67 before and after degradation.

reliability and effectiveness in the degradation of MB dye and CIP antibiotics. The photocatalyst performance shows no noticeable change after twenty cycles of visible light exposure, proving that the 30NFZ67 hybrid composite is a reliable and effective photocatalyst for the breakdown of MB dye and CIP antibiotics. Although there is a slight decline in activity, XRD analysis [Fig. 11(b)] reveals that the catalyst retains a high degree of crystallinity, underscoring its robust structural integrity throughout the process. In addition, the UV-Vis and IR spectra of the recycled catalyst correlate well with the pristine catalyst (Fig. S9). The pictorial representation of the 30NFZ67 catalyst before and after degradation is depicted in Fig. S10.

Conclusions

In this work, a series of NFZ67 composites with different weight percentages of NF amounts were synthesised. All the characterisations were employed for the analysis of the samples. The photocatalytic removal of MB and CIP under sunlight was carried out using simple and non-toxic catalysts. The 30NFZ67 nanocomposites exhibited the highest capacity for the degradation of MB (~98%) and CIP (~88%) in 30 mg L^{-1} and 10 mg L^{-1} solutions, respectively, under 60 min of visible light irradiation (sunlight). The degradation pathway follows a multilevel charge transfer mechanism and the pseudo first order kinetic model with rate constants of 0.03585 min^{-1} and 0.03852 for CIP and MB, respectively. Coupling of ZIF 67 with NF made a magnetic photocatalyst and thus well hindered the secondary pollution. The photocatalytic activity of the 30NFZ67 nanocomposite remained high over twenty cycles, indicating that the prepared sample can be ideal for long-term usage. This study could serve as a simple, promising strategy for modifying the photocatalytic performance of hybrid MOF-based nanomaterials for the efficient photodegradation of organic dyes and antibiotics in environmental wastewater.

Author contributions

A. P., N. D., and S. S. conducted the experimental work and data acquisition. R. S. was responsible for data validation and manuscript review.

Conflicts of interest

There are no conflicts to declare.

Data availability

The datasets generated and analysed during the current study are available from the corresponding author upon reasonable request. Data are available from the authors upon request.

Supplementary information (SI) is available. See DOI: https://doi.org/10.1039/d5ra09822j.

Acknowledgements

We sincerely acknowledge the Central Research Facility at Kalinga Institute of Industrial Technology (KIIT) for assistance with the characterization of our samples. We are also grateful to Dr Debendra Samal, IOP, for conducting the VSM analysis. This work is supported by DRDO/Grant no. LSRB.429/BTB/2024.

References

1 (*a*) K. Kumar, *RSC Appl. Interfaces*, 2025, **2**, 1288–1298; (*b*) Y. He, W. Bao, Y. Hua, Z. Guo, X. Fu, B. Na, D. Yuan, C. Peng and H. Liu, *RSC Adv.*, 2022, **12**, 5587–5594; (*c*) D. A. Giannakoudakis, P. Pauletto, M. Florent and T. J. Bandosz, *RSC Appl. Interfaces*, 2025, 1275–1287; (*d*) P. P. Cho, P. P. Mon, M. Kumar, S. Duvvuri, G. Madras, G.-P. Chang-Chien, S. Masimukku and S. Challapalli, *RSC Appl. Interfaces*, 2025, **2**, 1259–1274.

2 (*a*) C. McCullagh and P. K. Robertson, *Environ. Sci. Technol.*, 2006, **40**, 2421–2425; (*b*) H. C. Junqueira, D. Severino, L. G. Dias, M. S. Gugliotti and M. S. Baptista, *Phys. Chem. Chem. Phys.*, 2002, **4**, 2320–2328.

3 (*a*) S. Devi and S. Tyagi, *RSC Adv.*, 2022, **12**, 34951–34961; (*b*) Q. V. Vo, L. T. T. Thao, T. D. Manh, M. Van Bay, B.-T. Truong-Le, N. T. Hoa and A. Mechler, *RSC Adv.*, 2024, **14**, 27265–27273; (*c*) R. Dhir, B. Shah, A. Singh and N. Singh, *Dalton Trans.*, 2025, **54**, 8346–8356.

4 (*a*) M. LeBel, *Pharmacotherapy*, 1988, **8**, 3–30; (*b*) A. S. Giri and A. K. Golder, *RSC Adv.*, 2014, **4**, 6738–6745; (*c*) Z. Ma, X. Song, Z. Li, Y. Ren, J. Wang and Y. Liang, *Dalton Trans.*, 2024, **53**, 3797–3807.

5 Ł. Szczupak, A. Kowalczyk, D. Trzybiński, K. Woźniak, G. Mendoza, M. Arruebo, D. Steverding, P. Stączek and K. Kowalski, *Dalton Trans.*, 2020, **49**, 1403–1415.

6 (*a*) F. A. Sofi, M. H. Masoodi and N. Tabassum, *RSC Med. Chem.*, 2025, **16**, 1891–1922; (*b*) M. M. Ali, M. A. Eldeen, M. E. El Awady, A. A. Hamed, H. A. Abd Elhameed, A. Awadalla, M. Alshehri, H. M. Otifi, D. S. Alshaya and E. Fayad, *RSC Med. Chem.*, 2025, **16**, 3146–3157.

7 S. Badawy, Y. Yang, Y. Liu, M. A. Marawan, I. Ares, M.-A. Martinez, M.-R. Martínez-Larrañaga, X. Wang, A. Anadón and M. Martínez, *Crit. Rev. Toxicol.*, 2021, **51**, 754–787.

8 Z. Xiao, Y. Zheng, P. Chen, H. Liu, Z. Fang, J. Zhang, Z. Lin, Y. Zhang, J. Luo and W. Zhang, *Environ. Sci.: Nano*, 2022, **9**, 3110–3125.

9 (*a*) S. M. Zainab, M. Junaid, N. Xu and R. N. Malik, *Water Res.*, 2020, **187**, 116455; (*b*) J. Deng, G. Wu, S. Yuan, X. Zhan, W. Wang and Z.-H. Hu, *J. Photochem. Photobiol., A*, 2019,

371, 151–158; (*c*) S. P. Tripathy, S. Subudhi, A. Ray, P. Behera, A. Bhaumik and K. Parida, *Langmuir*, 2022, **38**, 1766–1780.
10 E. Mansor, H. abdallah and A. M. Shaban, *Environ. Qual. Manag.*, 2024, **34**, e22251.
11 A. Khrueakham, J. Masomboon, J. Roongruang and S. Sairiam, *RSC Adv.*, 2021, **11**, 17775–17788.
12 P. Czupryński, M. Płotka, P. Glamowski, W. Żukowski and T. Bajda, *RSC Adv.*, 2022, **12**, 5145–5156.
13 O. A. Ajala, S. O. Akinnawo, A. Bamisaye, D. T. Adedipe, M. O. Adesina, O. A. Okon-Akan, T. A. Adebusuyi, A. T. Ojedokun, K. A. Adegoke and O. S. Bello, *RSC Adv.*, 2023, **13**, 4678–4712.
14 L. Ge, M. Zhang, R. Wang, N. Li, L. Zhang, S. Liu and T. Jiao, *RSC Adv.*, 2020, **10**, 15091–15097.
15 J. Swain, A. Priyadarshini, S. Hajra, S. Panda, J. Panda, R. Samantaray, Y. Yamauchi, M. Han, H. J. Kim and R. Sahu, *J. Alloys Compd.*, 2023, **965**, 171438.
16 C. Zaharia, C.-P. Musteret and M.-A. Afrasinei, *Appl. Sci.*, 2024, **14**, 2184.
17 V. Khoo, S. F. Ng, C. Y. Haw and W. J. Ong, *Small*, 2024, **20**, 2401278.
18 I. Som, M. Roy and R. Saha, *ChemCatChem*, 2020, **12**, 3409–3433.
19 F. Mohamadpour and A. M. Amani, *RSC Adv.*, 2024, **14**, 20609–20645.
20 C. Xia, H. Wang, J. K. Kim and J. Wang, *Adv. Funct. Mater.*, 2021, **31**, 2008247.
21 G. Cai, P. Yan, L. Zhang, H.-C. Zhou and H.-L. Jiang, *Chem. Rev.*, 2021, **121**, 12278–12326.
22 C. Li, H. Zhang, M. Liu, F.-F. Lang, J. Pang and X.-H. Bu, *Ind. Chem. Mater.*, 2023, **1**, 9–38.
23 T. Wu, X.-j. Gao, F. Ge and H.-g. Zheng, *CrystEngComm*, 2022, **24**, 7881–7901.
24 B. He, Q. Zhang, Z. Pan, L. Li, C. Li, Y. Ling, Z. Wang, M. Chen, Z. Wang and Y. Yao, *Chem. Rev.*, 2022, **122**, 10087–10125.
25 D. De and P. Sahoo, *Dalton Trans.*, 2022, **51**, 9950–9965.
26 M. Usman, N. Iqbal, T. Noor, N. Zaman, A. Asghar, M. M. Abdelnaby, A. Galadima and A. Helal, *Chem. Rec.*, 2022, **22**, e202100230.
27 Z. Zheng, Z. Rong, H. L. Nguyen and O. M. Yaghi, *Inorg. Chem.*, 2023, **62**, 20861–20873.
28 (*a*) H. Sun, F. Wang, X. Li, J. Caro, H. Meng, N. Wang and Q. F. An, *Angew. Chem., Int. Ed.*, 2023, **62**, e202300262; (*b*) H. S. Jadhav, H. A. Bandal, S. Ramakrishna and H. Kim, *Adv. Mater.*, 2022, **34**, 2107072.
29 A. Nawaz, A. Rani, H. Zarrin and P. Saravanan, *Colloids Surf., A*, 2022, **642**, 128716.
30 (*a*) S. K. Paswan, P. Kumar, R. K. Singh, S. K. Shukla and L. Kumar, *Pollutants and Water Management: Resources, Strategies and Scarcity*, 2021, pp. 273–305; (*b*) X. Gao, X. Liu, Z. Zhu, X. Wang and Z. Xie, *Sci. Rep.*, 2016, **6**, 30543.
31 (*a*) H. Li, R. Chen, L. Sun, Y. Wang, Q. Liu, Q. Zhang, C. Xiao and Y. Xie, *Adv. Mater.*, 2024, **36**, 2408778; (*b*) L. D'Amario, L. J. Antila, B. Pettersson Rimgard, G. Boschloo and L. Hammarstrom, *J. Phys. Chem. Lett.*, 2015, **6**, 779–783.
32 (*a*) X.-Y. Guo, Z.-Q. Yang, J. Zhao and R. Liu, *Rare Met.*, 2024, **43**, 6751–6757; (*b*) T. Lan, H. Du, Y. Li, K. Qu, J. Zhao, X. Zhang, Y. Dong, Y. Zhang, X. Zhang and D. Zhang, *J. Alloys Compd.*, 2023, **943**, 169144; (*c*) F. Fatahi, S. Farhadi, A. Zabardasti and F. Mahmoudi, *Inorg. Chem. Commun.*, 2024, **162**, 112231.
33 S. Hajra, M. Sahu, A. M. Padhan, J. Swain, B. K. Panigrahi, H.-G. Kim, S.-W. Bang, S. Park, R. Sahu and H. J. Kim, *J. Mater. Chem. C*, 2021, **9**, 17319–17330.
34 A. Faraji, N. Mehrdadi, N. M. Mahmoodi, M. Baghdadi and A. Pardakhti, *J. Mol. Struct.*, 2021, **1223**, 129028.
35 V. Bharati, S. R. Patade, S. Bajaj, R. Parlikar, A. Keche and V. Sondur, *J. Phys.: Conf. Ser.*, 2020, **1644**, 012005.
36 J. Chang, Y. Wang, L. Chen, D. Wu, F. Xu, Z. Bai, K. Jiang and Z. Gao, *Int. J. Hydrogen Energy*, 2020, **45**, 12787–12797.
37 S. Lu, S. You, J. Hu, X. Li and L. Li, *RSC Adv.*, 2024, **14**, 7528–7539.
38 Y. Li, Z. Jin and T. Zhao, *Chem. Eng. J.*, 2020, **382**, 123051.
39 S. Joshi, M. Kumar, S. Chhoker, G. Srivastava, M. Jewariya and V. Singh, *J. Mol. Struct.*, 2014, **1076**, 55–62.
40 P. Sivakumar, R. Ramesh, A. Ramanand, S. Ponnusamy and C. Muthamizhchelvan, *Mater. Res. Bull.*, 2011, **46**, 2208–2211.
41 B. Pattengale, S. Yang, J. Ludwig, Z. Huang, X. Zhang and J. Huang, *J. Am. Chem. Soc.*, 2016, **138**, 8072–8075.
42 F. Wu, C. Zhou, G. Tai, Y. Ma, X. Yang, Y. Pan, J. Han, W. Xing and G. Wu, *ACS Appl. Nano Mater.*, 2023, **6**, 17814–17825.